



# Intelligent optimization method for seismic risk transfer parameters of high-speed railway track-bridge system

Wangbao Zhou<sup>a,b</sup>, Yingjie Li<sup>a</sup>, Lijun Xiong<sup>a,\*</sup>, Lizhong Jiang<sup>a,b,c</sup>, Zhaozhao Ma<sup>a</sup>

<sup>a</sup> School of Civil Engineering, Central South University, Changsha, China

<sup>b</sup> National Engineering Laboratory for High-speed Railway Construction, Changsha, China

<sup>c</sup> School of Civil Engineering, Hunan University of Science and Technology, Xiangtan, China

## ARTICLE INFO

### Keywords:

High-speed railway simply supported beam bridge  
Seismic risk transfer  
Intelligent optimization method  
Neural network  
Seismic performance

## ABSTRACT

Due to the widespread use of high-speed railway simply supported beam bridges in areas prone to high-risk earthquakes, the challenge of risk control for these bridges under seismic activity has become increasingly significant. Therefore, this study develops a finite element model to analyze the seismic response characteristics of the high-speed railway track-bridge system. It proposes a seismic risk transfer system for the high-speed railway track-bridge system. Then, an adaptive hybrid optimization algorithm is constructed, combining Particle Swarm Optimization (PSO) and Simulated Annealing (SA). This algorithm is used to create a neural network-based intelligent optimization method for configuring the parameters of the risk transfer device. In addition, the efficiency of the optimized risk transfer device is evaluated under various earthquake scenarios. The results indicated that the optimized seismic risk transfer device significantly enhances the seismic performance of the high-speed railway track-bridge system. The intelligent optimization method for the seismic risk transfer device parameters substantially reduces the stiffness requirements of the device, yielding economic benefits. The risk transfer device successfully mitigates the seismic risk to the bridge by transferring it to a more easily repairable embankment structure, thus reducing post-earthquake maintenance time and costs. These research results provide novel insights into the seismic design and optimization of bridges.

## 1. Introduction

China experiences frequent seismic activity across its vast territory, particularly at the intersection of earthquake fault zones in the west and high-intensity areas in the east, where high-speed railway bridges are exposed to significant seismic risks. Due to the critical nature of high-speed railway bridges, their structures must exhibit robust seismic performance to ensure the continuity and safety of bridge and track functions during earthquakes [1,2]. In current high-speed railway construction, multi-span simply supported beam bridges are prevalently employed for their simple construction and reasonable cost [3,4]. Therefore, the seismic performance of simply supported beam bridges has garnered considerable attention, and effectively mitigating seismic risks to ensure train operation is of substantial engineering importance [5,6].

In recent years, scholars have conducted extensive research on the seismic resistance of high-speed railway bridges. Yu et al. and Liu et al. [7,8] investigated the damage mechanisms of key bridge components

under seismic forces and identified that the bearing and sliding layer are particularly susceptible. Guo et al. [9] examined the seismic damage characteristics of various track structure components, while Zhou et al. [10] highlighted the vulnerability of bearing and lateral block in near-fault earthquakes. In addition, experimental studies by Feng et al. [11,12] indicated the failure modes and seismic performance influencing factors of shear rebar and lateral block in ballastless track system under seismic conditions. The constraint effect of the track system significantly impacts the longitudinal seismic response of bridges [13, 14], particularly in simply supported beam bridges with varying spans. The track structure can effectively diminish the structural seismic response [15,16]. Thus, accurately assessing the impact of track constraints on the seismic performance of bridge components is crucial for engineering seismic design [17].

Ductility design and seismic isolation device are two primary methods for controlling seismic risks in bridge structures. Early scholars introduced the concept of ductility seismic design, which absorbs energy and mitigates overall structural damage by anticipating the failure of

\* Corresponding author.

E-mail address: [ljxiong84@163.com](mailto:ljxiong84@163.com) (L. Xiong).

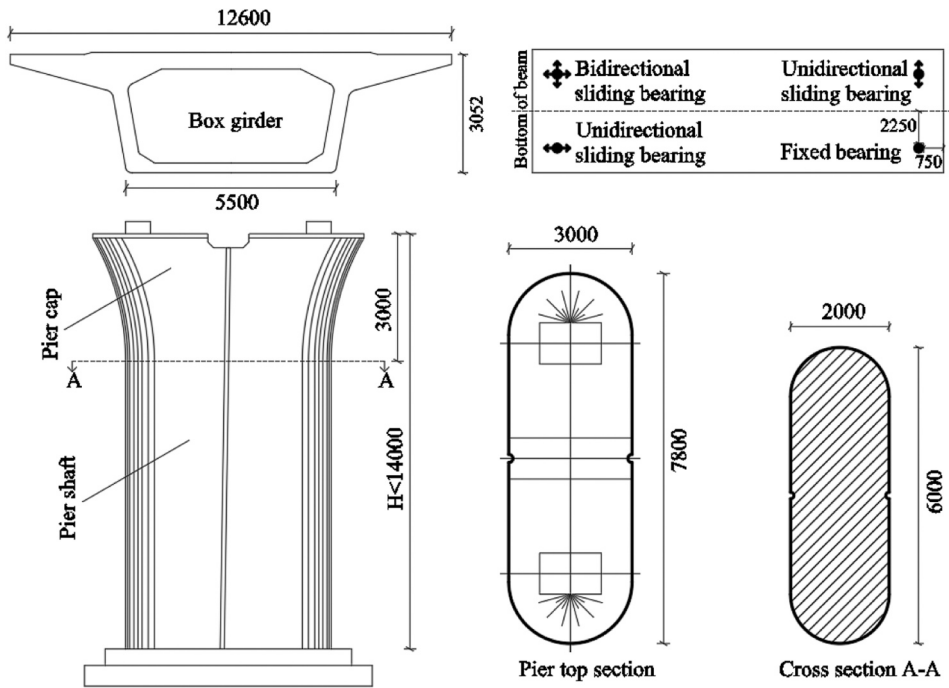


**Fig. 1.** High-speed railway bridge structure (unit: mm).

specific bridge parts [18–21]. Various innovative seismic isolation devices have emerged with advancements in seismic isolation technology for bridge structures. Friction pendulum bearings, metal damping tenons, and replaceable dampers are now widely utilized in bridge engineering, significantly enhancing the seismic performance of essential bridge components [22–27]. Although these advancements have substantially improved the seismic performance of local bridge components, challenges persist in managing seismic risks at the structural level, particularly in the comprehensive seismic design of high-speed railway track-bridge systems. Some scholars have attempted to propose seismic risk transfer strategy at the system level, such as achieving risk transfer and control through friction slab extension in the embankment section [28] or friction damper devices installed between spans [29]. Although these approaches demonstrate effectiveness in mitigating global seismic responses, they lack economic optimization. In addition, much of the current research on seismic isolation devices focuses primarily on optimizing individual component rather than considering the bridge's overall seismic requirements and economic feasibility [30–33].

Accordingly, this article presents the high-speed railway simply supported beam bridge system as the subject of study, proposes an intelligent optimization method based on a finite element model and an adaptive hybrid optimization algorithm, and achieves seismic risk transfer and control for the high-speed railway simply supported beam bridge system by configuring specific risk transfer device. The optimized risk transfer device significantly reduces the stiffness requirements while maintaining the effect of seismic risk transfer, enhancing economic benefits. The effectiveness of the risk transfer device in optimizing the seismic performance of bridges was validated through response analysis of the high-speed railway track-bridge system under various earthquake conditions. The data and codes used in this paper will be available on GitHub at <https://github.com/lyjd2000/Risk-Transfer> after the paper is published.

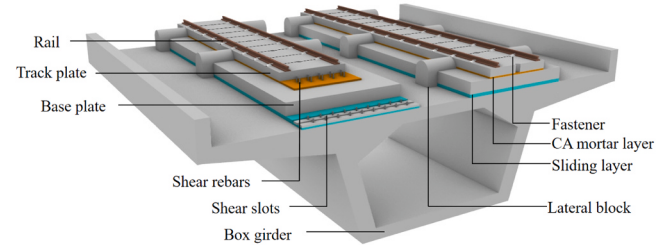


**Fig. 2.** High-speed railway track structure.

## 2. Finite element model of high-speed railway track-bridge system

### 2.1. High-speed railway track-bridge system model

The high-speed railway simply supported beam bridge system primarily comprises the bridge and track structures, as depicted in Figs. 1 and 2. The bridge structure utilizes standard prestressed concrete box girders with a span of 32.6 m, and the piers feature solid circular-end-type cross-section with a height of 9 m. Variable cross-section pier caps are installed at the top to enhance the bearing capacity. Each span's box girder is connected to the pier via four pot rubber bearings, specifically arranged as one fixed bearing, one bidirectional sliding bearing, and two unidirectional sliding bearings.

The track structure employs CRTS II slab ballastless track, which includes the base plate, track plate, and rail from bottom to top, configured as longitudinal continuous structures. The cross-sectional dimensions of the base plate and track plate are  $2.95 \times 0.19$  m and  $2.55 \times 0.2$  m, respectively. Shear slots on the surface of the beam, consisting of shear studs and grooves, restrict the movement of the base plate. Simultaneously, a 6 mm thick sliding layer is placed between the box girder and the base plate to mitigate structural stress from temperature variations. A CA mortar layer is positioned between the base and track plates, serving as a damping buffer to enhance train stability. Additionally, shear rebars are placed between the two above the box girder gap, reducing the deformation in the track structure caused by the

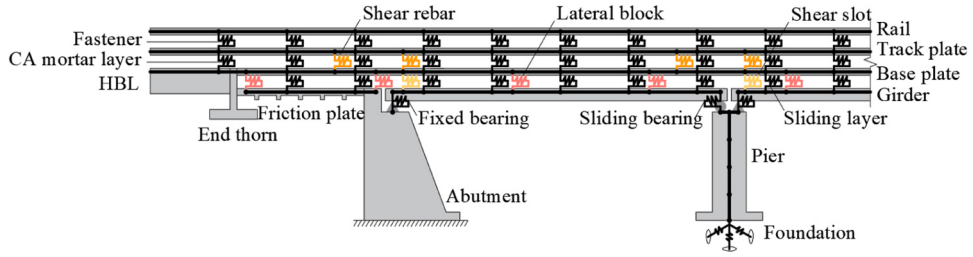


**Fig. 3.** Finite element model of high-speed railway track-bridge system.

**Table 1**  
Key material parameters of elastic components.

Component	Elastic modulus (N·mm <sup>-1</sup> )	Section area (mm <sup>2</sup> )	Mass density (kg·m <sup>-3</sup> )	Poisson ratio
Pier	$3.3 \times 10^4$	-	$2.5 \times 10^3$	0.2
Girder	$3.55 \times 10^4$	$1.28 \times 10^7$	$2.5 \times 10^3$	0.2
Base plate	$3.25 \times 10^4$	$5.6 \times 10^5$	$2.5 \times 10^3$	0.2
Track plate	$3.65 \times 10^4$	$5.1 \times 10^5$	$2.5 \times 10^3$	0.2
Rail	$2.06 \times 10^5$	$7.8 \times 10^3$	$7.85 \times 10^3$	0.3

girder cornering. Rail is secured on the track plate by fasteners, with adjacent fasteners longitudinally spaced at 0.65 m intervals. The rails utilize CHN60 rail, and the fasteners are WJ-8C type. In addition, lateral blocks are mounted on the box girder and friction plate to limit the lateral movement of the base plate. The longitudinal spacing between adjacent lateral blocks on the box girder and friction plate is set at 6.5

and 8 m, respectively.

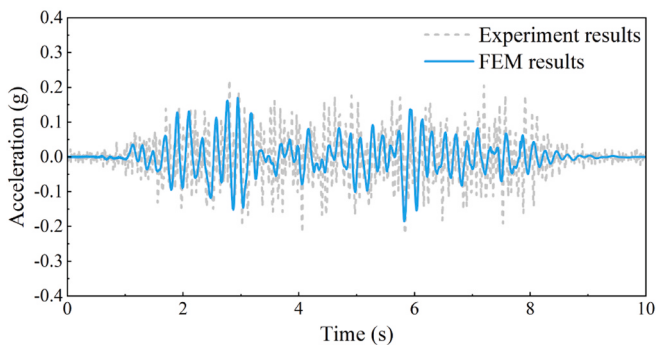
The embankment at both bridge ends includes the friction plate, end thorn, hydraulic bearing layer (HBL), and rock layer. The longitudinal lengths of the friction plate and HBL are 50 and 20 m, respectively. The friction plate gradually transmits the load from the upper track system to the lower roadbed and end thorn structure via interlayer friction. Laid beneath the friction plate and HBL, the rock layer helps disperse the load evenly and effectively reduces localized stress concentration. The end thorn structure, featuring a standard inverted T-shaped design with a height of 3.75 m, is placed between the friction plate and HBL. Its primary function is to restrict the longitudinal movement of the base plate, enhance the roadbed's constraint on the track system, and further improve the overall structure's stability.

A finite element model (FEM) of the high-speed railway track-bridge system is developed on the OpenSees dynamic analysis platform, as illustrated in Fig. 3. The bridge pier is simulated using displacement-based nonlinear element, which simulate the nonlinear deformation

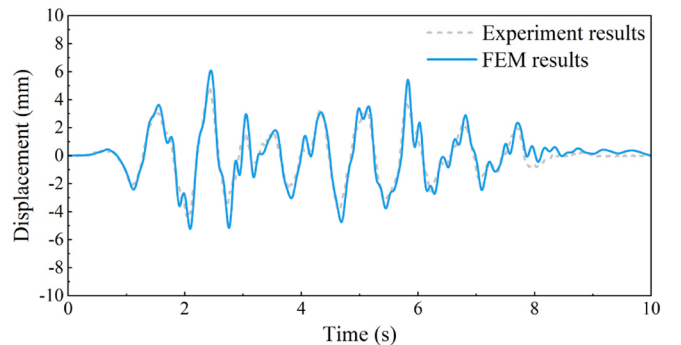
**Table 2**  
Key material parameters of nonlinear components.

Force-displacement curve	Component	<i>K</i> (kN·mm <sup>-1</sup> )		<i>D</i> (mm)	
		<i>x</i>	<i>y</i>	<i>x</i>	<i>y</i>
	Fixed bearing	500	500	2	2
	Sliding bearing	50	50	2	2
	Sliding layer	12	12	0.5	0.5
	CA mortar layer	84	84	0.5	0.5
	Fastener	4.5	4.5	2	2
	Shear slot	12208.3	12208.3	0.12	0.12
	Shear rebar	287.5	287.5	0.08	0.08
	Lateral block	-	226.5	-	2

Note: *x* represents longitudinal bridge direction, and *y* represents transverse bridge direction.

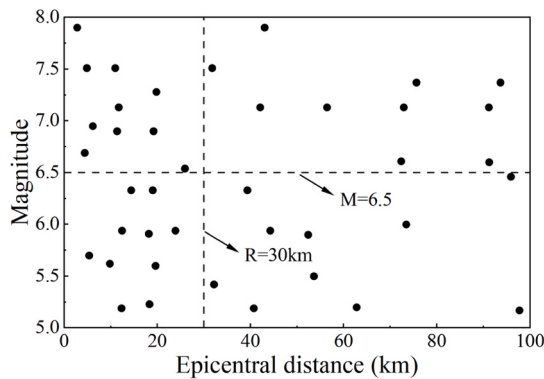


(a) Acceleration response

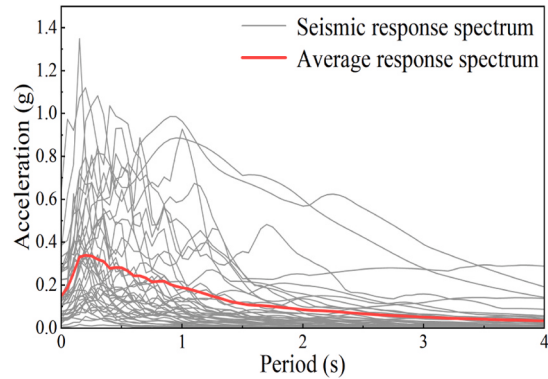


(b) Displacement response

**Fig. 4.** Finite element model verification [34,35].



(a) M-R distribution of selected seismic records



(b) Response spectra of selected seismic records

Fig. 5. Information on selected seismic records.

capacity of the bridge pier by integrating fiber cross-sections. In these cross-sections, the concrete fibers are represented using Concrete01 material, while the steel fibers utilize Steel02 material. During seismic activity, the potential damage to the box girder, base plate, track plate, and rail is not considered. Therefore, these components are simulated using ElasticBeamColumn element, with their principal parameters detailed in Table 1. Nonlinear components, such as pot rubber bearing, sliding layer, CA mortar layer, fastener, shear slot, shear rebar, and lateral block, are modeled using TwoNodeLink element to accurately represent these crucial components. In these components, nonlinear behavior in the horizontal direction employs ElasticPP bilinear material, while the vertical and rotational directions use Elastic material. The critical parameters for these nonlinear components are listed in Table 2.

In the simulation of the interaction between bridge piers and the foundation, three horizontal springs and three rotational springs are established, and the ZeroLength element is employed to model this interaction. The base plate, track plate, and rail are treated as fully consolidated at both ends of the bridge to simulate the constraint imposed by the embankment on the track structure. Damage to the bridge abutment is not considered and is assumed to have complete consolidation. In addition, the entire model utilizes Rayleigh damping, with a damping ratio set to 0.05. The FEM was validated through shake table tests using scaled model. The comparison between the numerical simulation results of acceleration and displacement responses and the experimental data is shown in Fig. 4. The good consistency between them verifies the FEM's effectiveness, indicating it can meet the analysis requirements of this study.

## 2.2. Selection of seismic records

The magnitude and range are crucial parameters that influence the structural response. This study employs the M-R (Magnitude-Range) method [36] to select seismic records. Given the significant randomness of seismic motion, to thoroughly assess the performance of structures under seismic activity, the selected seismic records must encompass a broad spectrum of magnitude and range. The selected magnitude range in this study spans from 5 to 8, with a range of 0–100 km, ensuring coverage of seismic events of varying intensities and proximities. The M-R method determined four quadrants based on magnitude and range, corresponding to large and small earthquakes and near-field and far-field seismic events. Specifically, a magnitude of 6.5 is the dividing line for large and small earthquakes, and 30 km is the dividing line for near and far fields. Following this classification, 40 seismic records were chosen from the PEER earthquake database, with ten seismic records in each quadrant to ensure an even data distribution, as depicted in Fig. 5 (a). Fig. 5(b) illustrates the acceleration response spectrum and average response spectrum of selected seismic records.

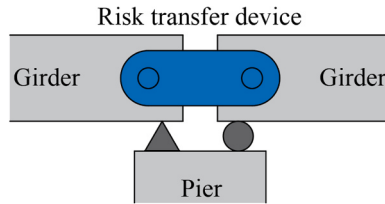


Fig. 6. Construction form of stiffness type limiter.

## 3. Seismic risk transfer analysis of high-speed railway track-bridge system

### 3.1. Seismic risk transfer device

A stiffness type limiter is utilized to achieve the objective of seismic risk transfer. The construction form of the stiffness type limiter is depicted in Fig. 6. The stiffness type limiter is positioned between the spans of the high-speed railway simply supported beam bridge. Its primary function is to provide adequate stiffness to enhance the connection between the box girders and augment the integrity of the multi-span high-speed railway simply supported beam bridge. At this time, the simply supported beam bridge resembles a continuous beam bridge, and the seismic response across each bridge span tends to be uniform. However, the stiffness variation from the bridge section to the embankment section is considerable, which can lead to significant differences in seismic response. This difference can be exploited to transfer seismic risk from the bridge to the embankment structure. In the finite element model of the high-speed railway track-bridge system, elastic element is employed to simulate the stiffness type limiter, and the ends of the spring are directly connected to the end of the girder element. When each span of the simply supported beam bridge is fully interconnected, the entire bridge section experiences coordinated forces. At this point, the stiffness type limiter theoretically attains the optimal risk transfer effect, and the corresponding maximum stiffness of the risk transfer device is  $k_{\max} = 4.56 \times 10^{12}$  N/m.

### 3.2. Analysis of seismic risk transfer effect

The seismic response of the bridge and track structures incorporating the risk transfer device was analyzed to evaluate the efficiency of the risk transfer device and compared to the seismic response outcomes of structures without such device. Given that the longitudinal direction of the bridge primarily facilitates the action of the risk transfer device, the seismic input for the model employs a longitudinally consistent excitation, the dynamic time history analysis interval is set to 0.02 s, and the

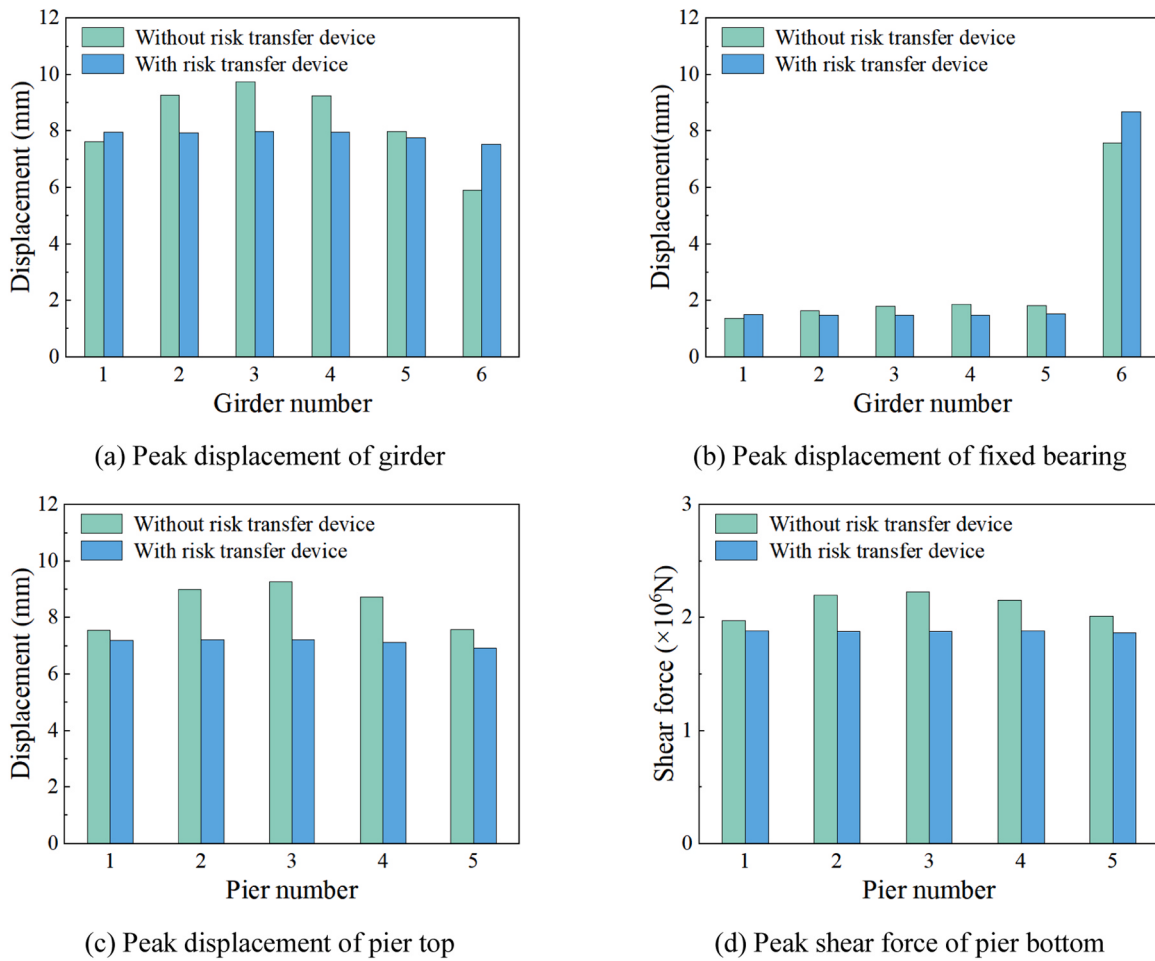


Fig. 7. Comparison of peak seismic response of bridge structure.

peak ground acceleration (PGA) is adjusted to 0.2 g. Due to spatial constraints, the time history analysis results from the "Hector Mine" seismic wave were chosen for presentation. Fig. 7 depicts the peak responses of the girder mid-span displacement, the fixed bearing displacement, the pier top displacement, and the pier bottom shear force of the high-speed railway simply supported beam bridge. It indicates that for bridge structure lacking the risk transfer device, the overall seismic response exhibits a decreasing trend from the center toward both ends. Upon implementing the risk transfer device, the seismic response at the center of the bridge structure significantly diminishes, while the displacement response at the mid-span and fixed bearing of the bridge side span increases. This indicates that the risk transfer device mitigates the seismic response of the middle spans of the upper structure of the bridge and amplifies the side span's seismic response to some extent, leading to a more uniform seismic response across the entire bridge.

Fig. 8 shows the comparison results of peak responses for the axial force of the base plate and displacements of the sliding layer, CA mortar layer, and shear rebars in the track structure. It indicates that the risk transfer device significantly reduces the overall level of seismic peak response of various components within the bridge section of the track structure. There is a noticeable increase in seismic response near the road-bridge transition section compared to structure without a risk transfer device. This is attributed to the additional stiffness imparted by the risk transfer device, which restricts the relative movement between the box girders. The seismic response of the track structure in the bridge section diminishes under earthquake forces. However, the heightened overall stiffness of the bridge results in an increased stiffness difference between the side span and the embankment section, elevating the

response of the embankment section under earthquake forces. This achieves the goal of transferring seismic risk of the track structure from the bridge section to the embankment section.

#### 4. Intelligent optimization method for seismic risk transfer system parameters

As the widespread application of high-speed railway simply supported beam bridges continues, earthquake risk management has increasingly become a focal point of bridge design and optimization. Although current seismic risk transfer devices have partially succeeded in dispersing and controlling bridge seismic risks, optimizing device parameters while considering economic benefits remains pressing. An intelligent optimization method for risk transfer system parameter configuration based on an adaptive hybrid optimization algorithm is proposed to address this need.

##### 4.1. Intelligent optimization model for seismic risk transfer system

The intelligent optimization model for seismic risk transfer system parameters presented in this article comprises three principal modules: training database construction, neural network model training, and optimizing via adaptive hybrid optimization algorithm. Each module functions collaboratively to achieve optimization objectives through multiple iterations. Fig. 9 reveals the detailed steps of the process, described as follows:

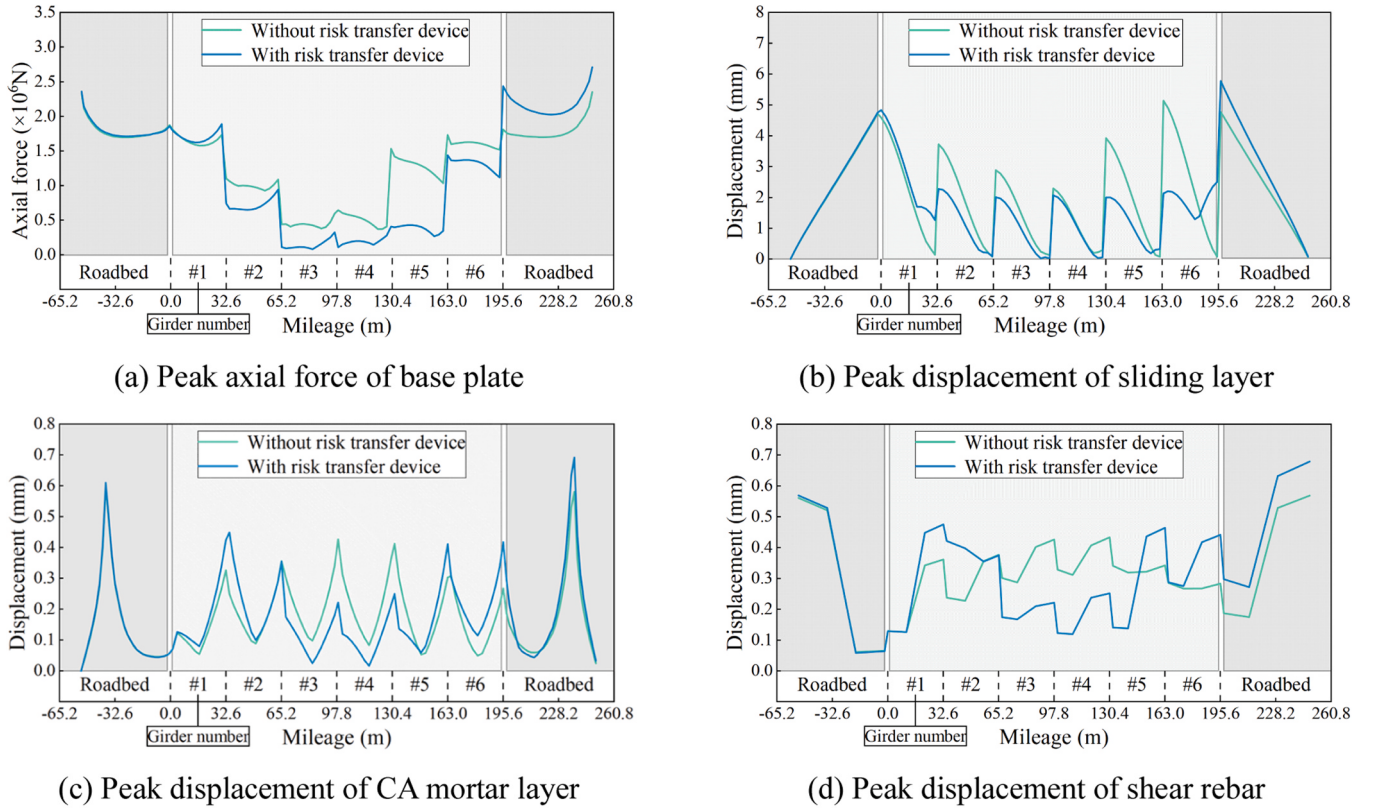


Fig. 8. Comparison of peak seismic response of track structure.

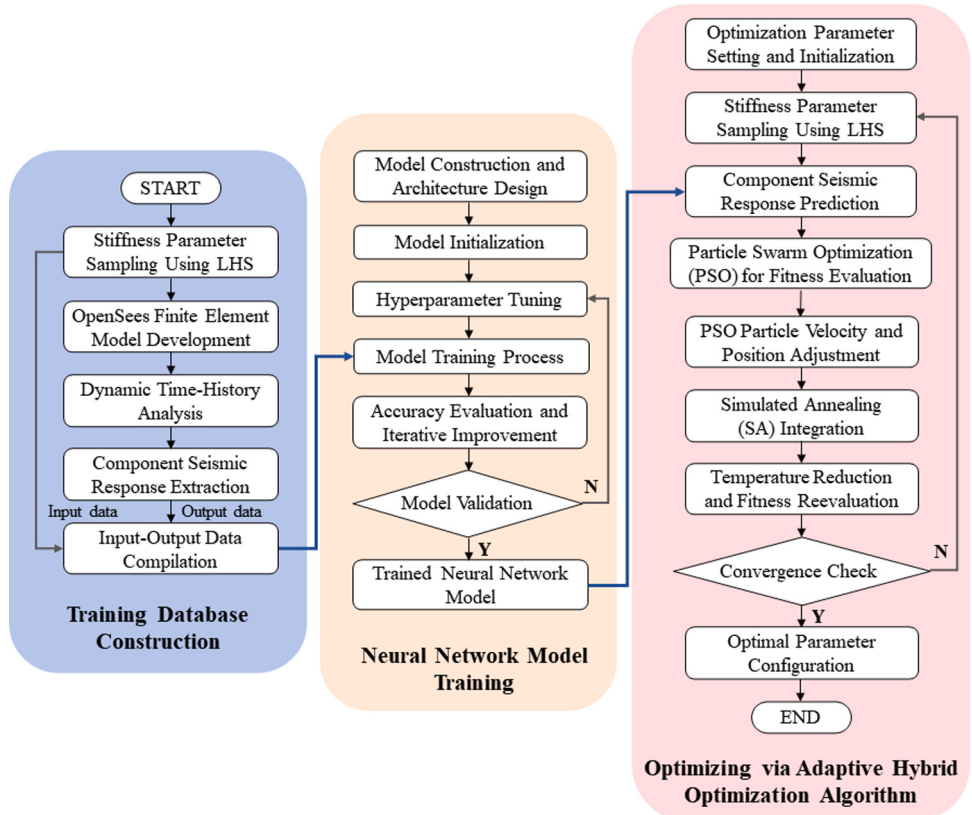


Fig. 9. Flowchart of parameters optimization method for seismic risk transfer system.

- (1) Training database construction. This study utilizes Latin Hypercube Sampling (LHS) to extract multiple parameter combinations, particularly those associated with stiffness parameters of risk transfer device, to ensure the model parameters encompass the possible design space. The primary aim of this step is to generate a series of representative parameter configurations through sampling technique, providing a data foundation for the subsequent optimization processes. Following this, a range of bridge finite element models with different risk transfer device parameters is created using OpenSees software to compute the seismic response of key bridge components. These response data, combined with corresponding stiffness parameters, are utilized to construct a comprehensive "input-output" database serving as the data source for subsequent neural network model training.
- (2) Neural network model training. This study innovatively incorporates rapid mapping neural network models into the optimization process to enhance the computational efficiency of optimization algorithm. This model uses the previously constructed database to establish a nonlinear mapping relationship between the risk transfer device's stiffness parameters and the track-bridge system's seismic response. During the neural network model's training process, a fully connected architecture comprising an input layer, an output layer, and multiple hidden layers was utilized to capture complex nonlinear relationships effectively. The training aims to adjust the network hyperparameters iteratively to ensure the model's performance evaluation coefficient R2 surpasses 95 %, confirming the model's precision in predicting the seismic response of critical components under varying stiffness parameters. The trained neural network model significantly accelerates the subsequent optimization process and enhances the accuracy of the outcomes.
- (3) Optimizing via adaptive hybrid optimization algorithm. This study introduces an adaptive hybrid optimization algorithm that merges the strengths of Particle Swarm Optimization (PSO) and Simulated Annealing (SA) to identify the global optimal solution in multidimensional nonlinear problems. Throughout the optimization process, the fitness function formulated considers both the track-bridge system's stiffness configuration and the seismic response requirements. The seismic response of the track-bridge system under each stiffness configuration parameter is swiftly predicted using the neural network model and evaluated in conjunction with the fitness function to determine the global optimal solution. The optimization process persists until the fitness value stabilizes.

#### 4.2. Adaptive hybrid optimization algorithm

An adaptive hybrid optimization algorithm for seismic risk transfer device parameters combines PSO with SA.

Particle Swarm Optimization (PSO) [37,38] completes the optimization process through iterative updates of particles' velocities and positions as they traverse the search space. The formulas for updating the velocity  $v_i$  and position  $x_i$  of particles are shown in Eqs. (1) and (2), where  $r_1$  and  $r_2$  are random numbers between [0,1];  $\omega$  is the inertia weight coefficient, which serves to establish a balance between global exploration and local exploitation;  $c_1$  is the individual learning factor that directs particles to fly toward the position  $P_{best}$  of the individual optimal solution;  $c_2$  is the social learning factor that directs particles to fly toward the position  $G_{best}$  of the population optimal solution.

$$v_i(n+1) = \omega v_i(n) + c_1 r_1 (P_{best,i}(n) - x_i(n)) + c_2 r_2 (G_{best}(n) - x_i(n)) \quad (1)$$

$$x_i(n+1) = x_i(n) + v_i(n+1) \quad (2)$$

The updated formula for the individual best position  $P_{best}$  and the population's best position  $G_{best}$  is as follows:

$$P_{best,i}(n+1) = \begin{cases} P_{best,i}(n), & f(x_i(n)) \leq f(P_{best,i}(n)) \\ x_i(n+1), & f(x_i(n)) > f(P_{best,i}(n)) \end{cases} \quad (3)$$

$$G_{best}(n+1) = \begin{cases} G_{best}(n), & f(P_{best,i}(n)) \leq f(G_{best}(n)) \\ P_{best,i}(n), & f(P_{best,i}(n)) > f(G_{best}(n)) \end{cases} \quad (4)$$

The values of  $c_1$ ,  $c_2$ , and  $\omega$  are adaptively updated with the number of iterations to enhance the algorithm's capacity to locate the global optimal solution. The maximum number of iterations set is  $n_{max}$ , and the maximum and minimum values of the individual learning factor  $c_1$  and the social learning factor  $c_2$  are set to 2.50 and 1.25, respectively. These values vary linearly with the number of iterations  $n$ , as demonstrated in Eqs. (5) and (6). The maximum and minimum values of the inertia weight coefficient  $\omega$  are set to 0.95 and 0.40, respectively. The negative hyperbolic tangent curve between [-4, 4] controls its variation, as depicted in Eq. (7).

$$c_1 = c_{1,max} - n(c_{1,max} - c_{1,min}) / n_{max} \quad (5)$$

$$c_2 = c_{2,min} - n(c_{2,min} - c_{2,max}) / n_{max} \quad (6)$$

$$\omega = 1/2(\omega_{max} + \omega_{min}) + 1/2(\omega_{max} - \omega_{min}) \bullet \tanh(8(n_{max} - n)/n_{max} - 4) \quad (7)$$

Although PSO has fewer hyperparameter dependencies and exhibits faster convergence speed, it is susceptible to becoming trapped in local optima within complex solution spaces. Therefore, the Simulated Annealing [39] is integrated with it. This algorithm uniquely accepts superior values during the simulation of temperature decrease and inferior values based on the probability generated by temperature variables, enhancing the likelihood of escaping local optima during the optimization process. This principle is known as the Metropolis criterion, as indicated in Eq. (8), where  $E_i(t)$  is the internal energy of the  $i$ -th particle at the  $t$ -th iteration;  $E_g$  is the optimal internal energy of the current population;  $T(t)$  is the current temperature;  $p_i(t)$  is the probability of accepting a new solution.

$$p_i(t) = \begin{cases} 1, & E_i(t) \geq E_g \\ \exp(- (E_i(t) - E_g) / T(t)), & E_i(t) < E_g \end{cases} \quad (8)$$

The variation of temperature  $T(t)$  is described in Eq. (9), with its initial temperature determined by the initial particle optimal value  $G_{best}$ , which decays with a specified cooling coefficient  $\mu$  after each iteration.

$$T(t) = \begin{cases} E(G_{best}) / \log(0.2), & t = 1 \\ T(t-1)\mu, & t > 1 \end{cases} \quad (9)$$

The SA iteration algorithm is incorporated into each iteration of PSO to optimize the solution generated. Each iteration simulates the movement of particles within the solid as the temperature decreases. Starting from  $G_{best}$ , it aims to generate new solutions around this value. It is then assessed whether the new solution generated by this perturbation replaces the global optimal solution according to the Metropolis criterion. The adaptive hybrid optimization algorithm developed from this approach can swiftly converge and fulfill the optimization objectives, offering considerable benefits for the complex nonlinear optimization problem addressed in this study.

Within the framework outlined above, the adaptive hybrid optimization algorithm assesses solution quality in each iteration by constructing a fitness function based on two optimization objectives:

Optimization objective 1: Minimize the stiffness configuration of risk transfer device as much as possible to enhance economic efficiency.

Optimization objective 2: Ensure that the optimized seismic response approximates as closely as possible to the seismic response under the maximum stiffness configuration, maintaining the seismic performance.

The fitness function considers these two optimization objectives, and the corresponding formula is as follows:

$$fitness = \beta \bullet f_1 + \gamma \bullet f_2 \quad (10)$$

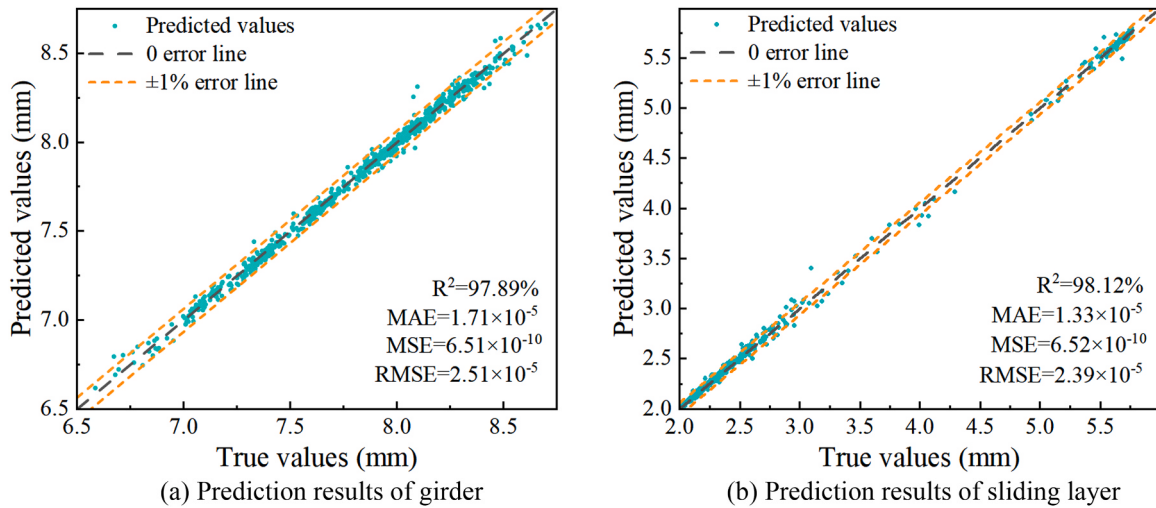


Fig. 10. Neural network prediction results.

where  $f_1$  and  $f_2$  are the fitness values for optimization objectives 1 and 2, respectively, calculated using Eq. (11) and (12). The parameter  $\beta$  controls the degree of stiffness reduction while  $\gamma$  ensures the accuracy of the seismic response to balance the weights between these objectives. The algorithm progressively identifies the optimal solution during the iteration process through dynamic adjustments of these coefficients.

$$f_1 = G\left(\sum_{i=1}^5 k_i\right) \quad (11)$$

$$f_2 = G(R^2(|y_1|, |\hat{y}_1|)) + \dots + G(R^2(|y_n|, |\hat{y}_n|)) \quad (12)$$

where  $k_i$  is the stiffness value of the  $i$ -th risk transfer device;  $y_n$  and  $\hat{y}_n$  are the seismic response value of the component under the maximum stiffness configuration and a specific set of stiffness configurations during the iteration process, respectively;  $n$  is the sequence number of the critical component;  $G(\cdot)$  is a specially defined function utilized to moderate the influence of various calculated values on the final fitness value, extracting the top three significant digits of the independent variable and converting its value to between [0,10].

## 5. Case study on optimization of seismic risk transfer system

### 5.1. Parameter setting of adaptive hybrid optimization algorithm

A case study was conducted on optimizing risk transfer device parameters utilizing a six-span high-speed railway track-bridge system to assess the efficiency of the intelligent optimization method presented in this research. The basic structural parameters and the track-bridge system's finite element model were established depending on Section 2.

The performance of neural network models depends on the diversity and scale of the database used during training. For this purpose, while constructing a neural network training database, LHS was employed to generate 1000 sets of risk transfer device parameters with varying stiffness configurations, and based on these, 1000 OpenSees finite element models were developed. Then, a "stiffness parameters-key

component seismic response" database was created through dynamic time history analysis for neural network training and optimization. An 8-layer fully connected neural network was constructed, featuring six hidden layers to enhance the accuracy of model predictions. The neuron counts were 8, 18, 64, 64, 18, and 8, respectively, utilizing the ELU activation function. The model's optimizer was Adam, the loss function was MSE, and the number of training iterations was set to 1000.

During the optimization process, the peak displacement of the girder mid-span and the sliding layer served as critical metrics for evaluating the differences in seismic performance of the track-bridge system under various stiffness configurations. The optimization goal was to reduce the stiffness configuration of risk transfer device while ensuring that the seismic performance of the bridge and track systems did not significantly deteriorate. Therefore, in the hybrid optimization algorithm, the search space of the PSO algorithm was set within the effective range of stiffness values ( $4.56 \times 10^8$  to  $4.56 \times 10^{10}$  N/m) [16], with the initial velocity set at 10 % of this search space ( $4.5144 \times 10^9$  N/m). The number of particles was set at 100, and the data dimension corresponded to five stiffness values to be optimized. During each iteration, 100 rows and five columns of stiffness parameter matrices were randomly generated as inputs for the optimization algorithm. The maximum number of iterations for the algorithm was 500, with the SA algorithm set at 100 iterations. The algorithm was to run the PSO algorithm once and the SA algorithm 100 times per iteration to optimize the solution. If the global optimal solution showed insignificant changes over 20 iterations, the algorithm would terminate and output the optimal solution.

### 5.2. Parameter optimization results

The optimization of the stiffness parameters of seismic risk transfer device is based on the proposed intelligent optimization method. Fig. 10 depicts the prediction results of the trained neural network model for the peak displacement of the girder mid-span and the sliding layer. The main evaluation metrics and scores of the model are shown in Table 3 [40]. Most data points fall within the  $\pm 1\%$  error range. The  $R^2$  evaluation values for the mid-span and sliding layer response prediction

**Table 3**  
Evaluation metrics and scores.

Metrics	$R^2$	MAE	MSE	RMSE
Formula	$1 - \frac{\sum_{i=1}^N (x_i - \hat{x}_i)^2}{\sum_{i=1}^N (x_i - \bar{x})^2}$	$\frac{1}{N} \sum_{i=1}^N  x_i - \hat{x}_i $	$\frac{1}{N} \sum_{i=1}^N (x_i - \hat{x}_i)^2$	$\sqrt{\frac{1}{N} \sum_{i=1}^N (x_i - \hat{x}_i)^2}$
Girder	97.89 %	$1.71 \times 10^{-5}$	$6.51 \times 10^{-10}$	$2.51 \times 10^{-5}$
Sliding layer	98.12 %	$1.33 \times 10^{-5}$	$6.52 \times 10^{-10}$	$2.39 \times 10^{-5}$

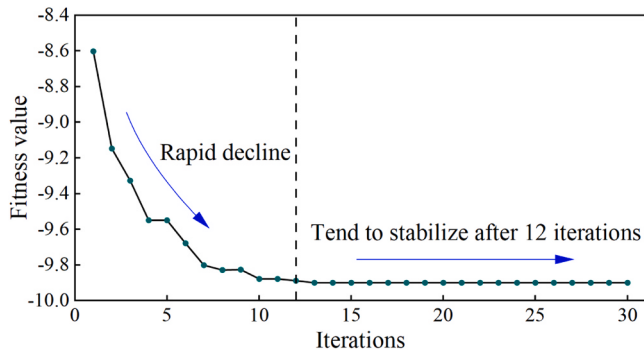


Fig. 11. Iterative update of fitness value for the optimal solution.

results are 97.89 % and 98.12 %, respectively. This demonstrates that the discrepancy between the predicted and actual values of the neural network model is minimal under different stiffness parameters, confirming the model's high accuracy and applicability.

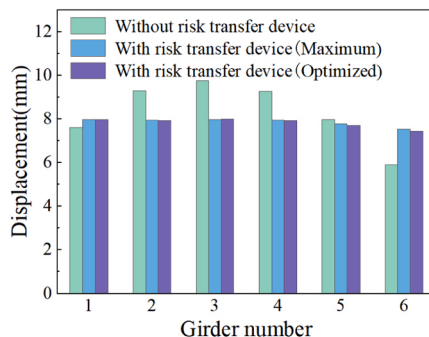
After 12 iterations, the fitness value stabilized during the optimization process, as shown in Fig. 11, indicating that the proposed optimization method is highly efficient. The optimal stiffness parameters are detailed in Table 4. This method significantly reduced the stiffness value by 2–3 orders of magnitude, effectively minimizing the stiffness configuration of the risk transfer device.

### 5.3. Seismic response assessment of optimized high-speed railway track-bridge system

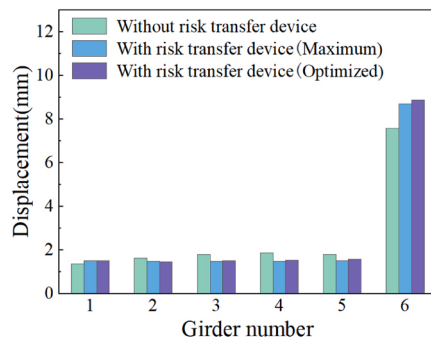
Forty selected seismic records were utilized to perform multiple dynamic time history analyses of the high-speed railway track-bridge system to assess the seismic risk transfer effect of the optimized stiffness configuration under various earthquake conditions. Fig. 12 displays the seismic response comparison of critical components of the bridge (girder mid-span, fixed bearing, pier top, and pier bottom) before and after optimization for the "Hector Mine" earthquake action. It demonstrates that compared to the maximum stiffness configuration, the peak displacement of the girder mid-span and the fixed bearing in the optimized high-speed railway track-bridge system remains relatively unchanged. The displacement at the top of the pier and the shear force at the bottom exhibit slight increases, but these are within a manageable range. This suggests that the optimized stiffness configuration, like the maximum stiffness configuration, can effectively mitigate the seismic response of the girder mid-span, the bearing, and the pier and balance the seismic risks across different bridge positions. Fig. 13 illustrates the seismic response comparison of each track structure component (base plate, sliding layer, CA mortar layer, and shear rebar) before and after optimization. It indicates that the response curves of the optimized stiffness configuration and the maximum stiffness configuration align closely. The responses of various key components in the track system show no substantial changes post-optimization, successfully achieving the risk transfer objective.

**Table 4**  
Optimization results.

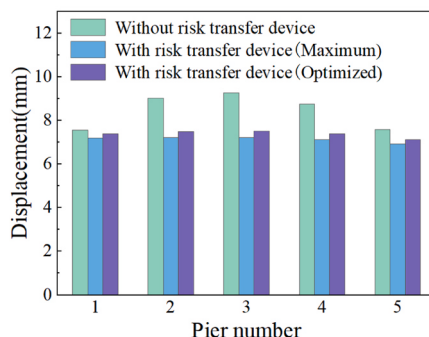
Results (N/m)	$k_1$	$k_2$	$k_3$	$k_4$	$k_5$
Maximum stiffness	$4.56 \times 10^{12}$				
Optimized stiffness	$2.15 \times 10^{10}$	$7.94 \times 10^9$	$2.17 \times 10^{10}$	$2.77 \times 10^{10}$	$2.21 \times 10^{10}$



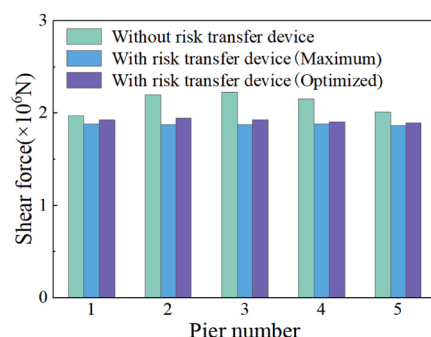
(a) Peak displacement of girder



(b) Peak displacement of fixed bearing



(c) Peak displacement of pier top



(d) Peak shear force of pier bottom

Fig. 12. Comparison of optimization results on peak seismic response of bridge structure.

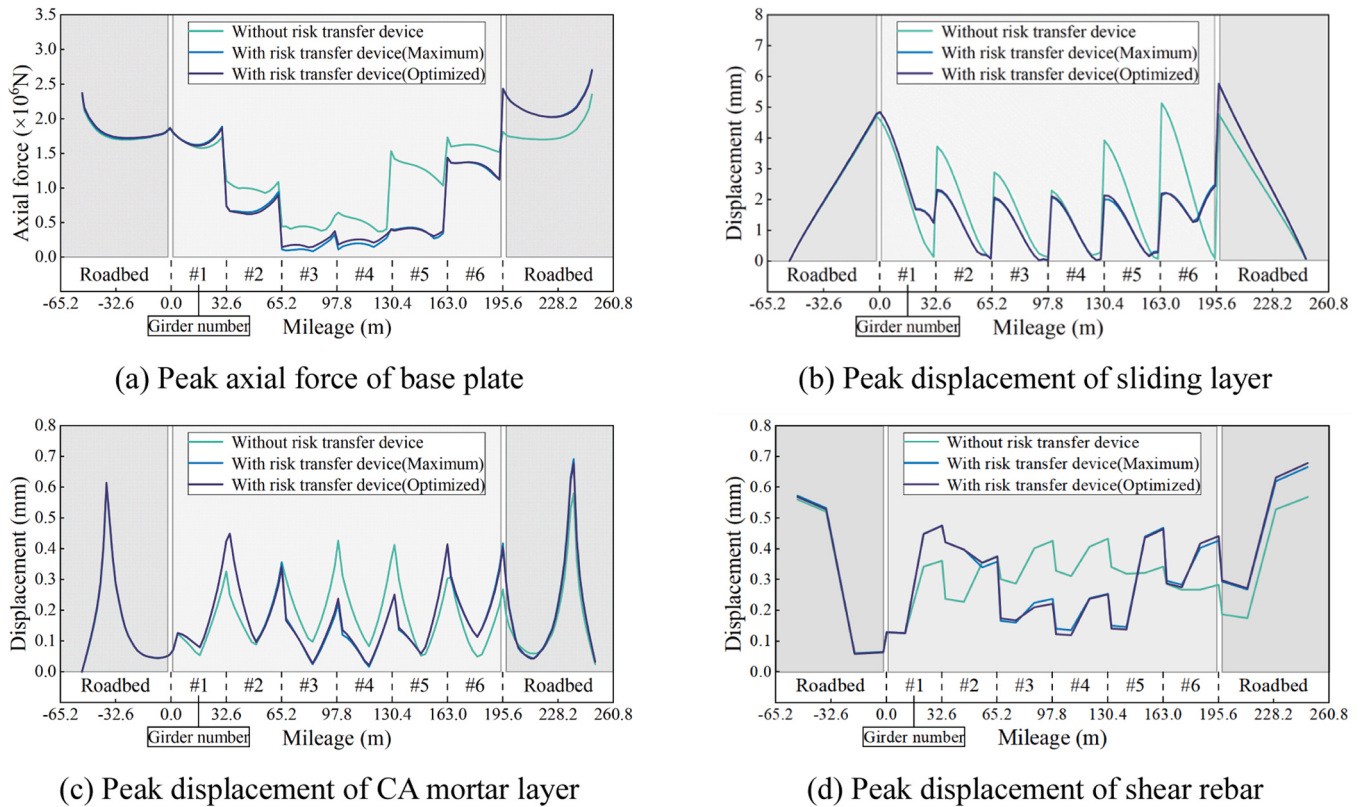


Fig. 13. Comparison of optimization results on peak seismic response of track structure.

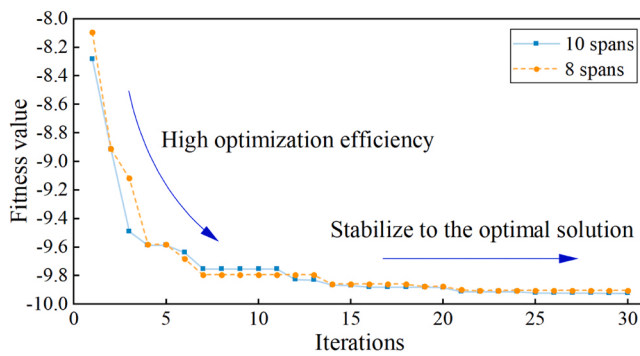
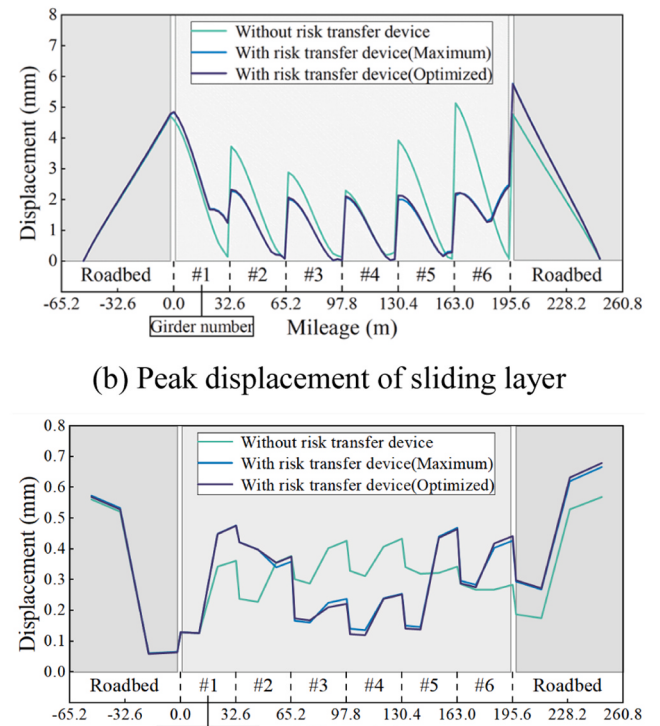


Fig. 14. Iterative update of fitness value for the optimal solution.

#### 5.4. Research on the applicability of the optimization method

To further explore the applicability of the optimization method to bridges with different numbers of spans, the intelligent optimization model was employed to optimize the stiffness configuration of the risk transfer system for 8-span and 10-span bridges. The iterative process of fitness value and the results of the optimal solutions are presented in Fig. 14 and Table 5. It can be observed that the optimization method exhibits extremely high efficiency within the first 10 iterations and then gradually stabilizes, successfully achieving the optimization objective. The order of magnitude of the optimal solution is consistent with that of



(d) Peak displacement of shear rebar

the 6-span bridge, attaining the expected economic benefits.

The seismic peak responses of components under the obtained optimal stiffness configuration were compared with the maximum stiffness configuration and without the risk transfer device. The comparison results of four components, namely the girder mid-span, the pier top, the base plate, and the sliding layer, are shown in Figs. 15 and 16. In terms of the components of the bridge structure, the seismic peak response of the optimized stiffness has a slight increase over that of the maximum stiffness, with the difference is within millimeters. Regarding the axial force of the base plate in the track structure, the response curves of the optimized stiffness and the maximum stiffness show a slight difference at positions far from the embankment. The response curves of the two configurations are almost identical for the sliding layer displacement. These results are consistent with the patterns of 6-span bridges. The optimized stiffness configuration still effectively achieves the risk transfer goal, indicating that the proposed risk transfer strategy and optimization method have excellent applicability to bridges with different configurations.

#### 6. Conclusion

Based on the high-speed railway track-bridge system, an intelligent optimization method for seismic risk transfer system is developed, indicating the impact of different configuration parameters of risk transfer device on the seismic response of the track-bridge system. These device parameters are optimized using an adaptive hybrid optimization algorithm, and the efficiency of this optimization approach is

**Table 5**  
Optimization results.

Results (N/m)	$k_1$	$k_2$	$k_3$	$k_4$	$k_5$	$k_6$	$k_7$	$k_8$	$k_9$
8-span	$1.43 \times 10^{10}$	$1.03 \times 10^{10}$	$4.60 \times 10^9$	$7.87 \times 10^9$	$1.64 \times 10^{10}$	$2.34 \times 10^{10}$	$3.06 \times 10^{10}$		
10-span	$1.67 \times 10^{10}$	$9.74 \times 10^9$	$7.93 \times 10^9$	$4.69 \times 10^9$	$5.56 \times 10^9$	$1.69 \times 10^{10}$	$1.37 \times 10^{10}$	$1.82 \times 10^{10}$	$3.48 \times 10^{10}$

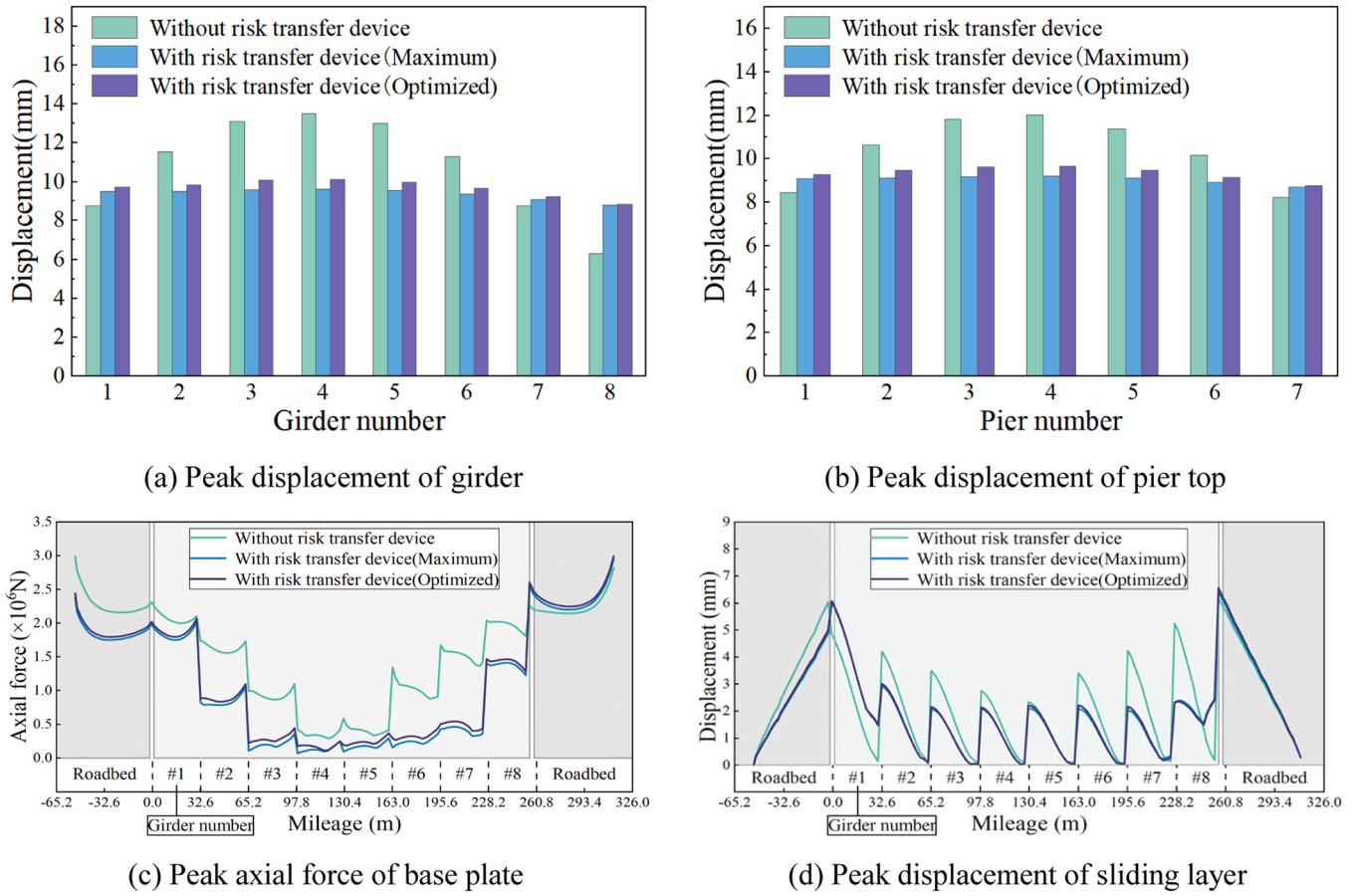


Fig. 15. Comparison of optimization results on peak seismic response of 8-span bridge.

substantiated through case analysis. The main conclusions are as follows:

- (1) The optimized risk transfer device ensures the seismic risk transfer effect of the high-speed railway track-bridge system while significantly reducing device stiffness requirements. The optimized risk transfer device offers economic advantages.
- (2) The optimized risk transfer device effectively manages the seismic response of bridge structure while redistributing some bridge seismic risks to more readily repairable embankment structure, thus substantially reducing post-earthquake maintenance time and costs.
- (3) The adaptive hybrid optimization algorithm, based on PSO and SA, can effectively find the global optimal solution for multidimensional nonlinear stiffness parameters. It has good applicability to bridges with different span configurations. These research findings can provide a theoretical reference for seismic risk transfer optimization methods of high-speed railway track-bridge systems.

The proposed intelligent optimization method considers both seismic performance and economic benefits, effectively optimizing the stiffness parameters of the risk transfer device to achieve the goal of seismic risk transfer. However, this study still has several limitations: (1) The risk transfer strategy and the intelligent optimization method have only been studied for the simply supported beam bridge type, and its effectiveness and applicability for bridges with different structural types require further exploration. (2) While the fully connected neural network has demonstrated effectiveness in capturing nonlinear relationships, it still has optimization potential in efficiency and generalization for complex scenarios. Advanced machine learning architectures (e.g., gradient

boosting machine [41]) could be explored to enhance model robustness and parameter optimization accuracy. (3) To enhance the practical engineering applicability of risk transfer device, it is essential to investigate more reasonable and efficient device structure forms and layout methods. Meanwhile, applying the optimized parameters to practical engineering designs faces significant challenges, particularly in balancing optimization effectiveness, economic costs, and construction feasibility during multi parameter optimization.

#### CRediT authorship contribution statement

**Xiong Lijun:** Writing – review & editing, Software, Methodology, Conceptualization. **Li Yingjie:** Writing – review & editing, Writing – original draft, Formal analysis, Data curation. **Zhou Wangbao:** Writing – review & editing, Resources, Project administration, Funding acquisition. **Ma Zhaozhao:** Writing – original draft, Validation, Data curation. **Jiang Lizhong:** Supervision, Resources, Project administration, Funding acquisition.

#### Declaration of Competing Interest

The authors declare that there are no conflicts of interest regarding the publication of this paper. This research was conducted in the absence of any commercial or financial relationships that could be construed as a potential conflict of interest. The authors have no affiliations with or involvement in any organization or entity with any financial interest, or non-financial interest in the subject matter or materials discussed in this manuscript.

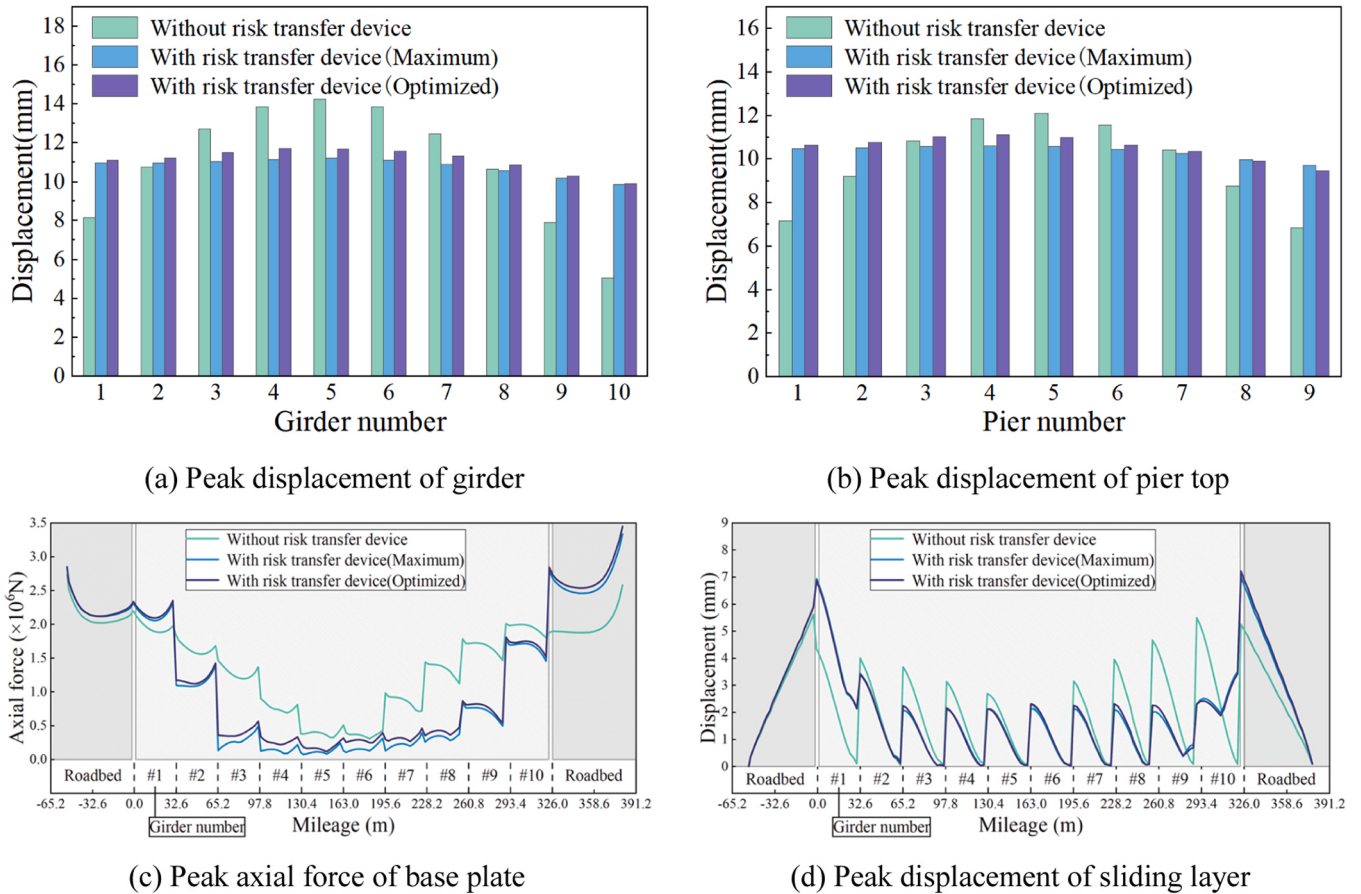


**Fig. 16.** Comparison of optimization results on peak seismic response of 10-span bridge.

## Acknowledgments

The research described in this paper was financially supported by the National Natural Science Foundations of China (52078487, 52178180),

Hunan Province Science and Technology Talent Lifting Project (2022TJ-Y10), Frontier cross research project of Central South University (2023QYJC006), the Science and Technology Development Fund (SKL-IOTSC(UM)-2021–2023).

## Appendix

**Table.A**

Detailed information on selected seismic records ([Section 2.2](#)).

No.	Earthquake Name	Year	Station Name	Magnitude	Rrup (km)
1	Hollister–01	1961	Hollister City Hall	5.60	19.56
2	Imperial Valley–08	1979	Westmorland Fire Sta	5.62	9.76
3	Anza (Horse Canyon)–01	1980	Anza - Terwilliger Valley	5.19	12.28
4	Mammoth Lakes–03	1980	Long Valley Dam (Downst)	5.91	18.13
5	Mammoth Lakes–04	1980	Convict Creek	5.70	5.32
6	Mammoth Lakes–06	1980	Bishop - Paradise Lodge	5.94	23.86
7	Mammoth Lakes–06	1980	Convict Creek	5.94	12.39
8	Victoria_ Mexico	1980	Cerro Prieto	6.33	14.37
9	Victoria_ Mexico	1980	Chihuahua	6.33	18.96
10	Coalinga–08	1983	Sulphur Baths (temp)	5.23	18.28
11	Northwest Calif–01	1938	Ferndale City Hall	5.50	53.58
12	Southern Calif	1952	San Luis Obispo	6.00	73.41
13	Northern Calif–07	1975	Shelter Cove_ Sta A	5.20	62.76
14	Livermore–02	1980	Antioch - 510 G St	5.42	32.13
15	Anza (Horse Canyon)–01	1980	Borrego Air Ranch	5.19	40.67
16	Mammoth Lakes–06	1980	Benton	5.94	44.21
17	Victoria_ Mexico	1980	SAHOP Casa Flores	6.33	39.30
18	Big Bear–01	1992	Puerta La Cruz	6.46	95.86
19	Northwest China–01	1997	Xiker	5.90	52.36

(continued on next page)

**Table A (continued)**

No.	Earthquake Name	Year	Station Name	Magnitude	Rrup (km)
20	Mohawk Val_Portola	2001	Carson City	5.17	97.70
21	Imperial Valley—02	1940	El Centro Array #9	6.95	6.09
22	Superstition Hills—02	1987	Salton Sea Wildlife Refuge	6.54	25.88
23	Erzican_Turkey	1992	Erzincan	6.69	4.38
24	Landers	1992	Coolwater	7.28	19.74
25	Kobe_Japan	1995	Amagasaki	6.90	11.34
26	Kobe_Japan	1995	Shin-Osaka	6.90	19.15
27	Kocaeli_Turkey	1999	Gebze	7.51	10.92
28	Kocaeli_Turkey	1999	Yarimca	7.51	4.83
29	Hector Min	1999	Hector	7.13	11.66
30	Denali_Alaska	2002	TAPS Pump Station #10	7.90	2.74
31	Northwest Calif—02	1941	Ferndale City Hall	6.60	91.22
32	Kocaeli_Turkey	1999	Goynuk	7.51	31.74
33	Manjil_Iran	1990	Abhar	7.37	75.58
34	Manjil_Iran	1990	Tonekabun	7.37	93.62
35	Hector Mine	1999	Desert Hot Springs	7.13	56.40
36	Hector Mine	1999	Mentone Fire Station #9	7.13	91.15
37	Hector Mine	1999	Snow Creek	7.13	72.88
38	Hector Mine	1999	Twenty-nine Palms	7.13	42.06
39	Denali_Alaska	2002	R109 (temp)	7.90	43.00
40	Tottori_Japan	2000	HRS015	6.61	72.30

Notes: Rrup represents the closest distance (orthogonal) to the fault plane.

## References

- [1] Jiang L, Yu J, Zhou W, et al. Applicability analysis of high-speed railway system under the action of near-fault ground motion. *Soil Dyn Earthq Eng* 2020;139:106289.
- [2] Jiang L, Zhong B, Zhou W, et al. Simplified linear analysis model of longitudinal constraint effect of high-speed railway simply-supported bridge under frequent earthquake. *Bull Earthq Eng* 2024;22(4):1827–53.
- [3] He X, Wu T, Zou Y, et al. Recent developments of high-speed railway bridges in China. *Struct Infrastruct Eng* 2017;13(12):1584–95.
- [4] Yan B, Dai G, Hu N. Recent development of design and construction of short span high-speed railway bridges in China. *Eng Struct* 2015;100:707–17.
- [5] Li H, Yu Z, Mao J, et al. Nonlinear random seismic analysis of 3D high-speed railway track-bridge system based on OpenSEES. *Structures* 2020;24:87–98.
- [6] Zhan J, Wang C, Yan Y, et al. Modal analysis and condition evaluation of substructures for simply supported high-speed railway bridge based on a simplified model. *J Bridge Eng* 2022;27(8):04022058.
- [7] Yu J, Jiang L, Zhou W, et al. Component damage and failure sequence of track-bridge system for high-speed railway under seismic action. *J Earthq Eng* 2023;27(3):656–78.
- [8] Liu L, Jiang L, Zhou W, et al. Analysis of seismic damage features of HSR CRTS III SBT simply supported bridge system. *Arch Civ Mech Eng* 2023;23:76.
- [9] Guo W, Hu Y, Hou W, et al. Seismic damage mechanism of CRTS-II slab ballastless track structure on high-speed railway bridges. *Int J Struct Stab Dyn* 2020;20(1):2050011.
- [10] Zhou G, Zhu Z, Tang Y, et al. Seismic scenario reproduction and damage mechanism analysis of Liuhuanggou Bridge under near-fault earthquake. *Bull Earthq Eng* 2023;21(13):6091–120.
- [11] Feng Y, Jiang L, Zhou W, et al. Experimental investigation on shear steel bars in CRTS II slab ballastless track under low-cyclic reciprocating load. *Constr Build Mater* 2020;255:119425.
- [12] Feng Y, Li J, He B, et al. Experimental study on seismic performance of CRTS II slab-type ballastless track lateral block of HSRs. *J Earthq Eng* 2024;1–22.
- [13] Zhou W, Peng D, Liu L, et al. Transverse seismic analysis of high-speed railway bridge in China based on a simplified calculation model. *J Cent South Univ* 2023;30:351–64.
- [14] Cui S, Guo C, Su J, et al. Seismic fragility and risk assessment of high-speed railway continuous-girder bridge under track constraint effect. *Bull Earthq Eng* 2019;17(3):1639–65.
- [15] Zhang Y, Jiang L, Zhou W, et al. Reduction of the longitudinal seismic response of high-speed railway multi-span simply-supported bridges by the track constraint. *J Earthq Eng* 2023;28(2):402–23.
- [16] Zhang Y, Jiang L, Zhou W, et al. Control of difference of seismic response across different spans of high-speed railway multi-spans simply supported bridge. *Bull Earthq Eng* 2022;20(12):6919–41.
- [17] Wei B, Wang W, Wang P, et al. Seismic responses of a high-speed railway (HSR) bridge and track simulation under longitudinal earthquakes. *J Earthq Eng* 2022;26(9):4449–70.
- [18] Jara M, Jara JM, Olmos BA. Seismic energy dissipation and local concentration of damage in bridge bents. *Struct Infrastruct Eng* 2011;9(8):794–805.
- [19] Piras S, Palermo A, Saiedi MS. State-of-the-art of posttensioned rocking bridge substructure systems. *J Bridge Eng* 2022;27(3):03122001.
- [20] Nie L, Jiang L, Zhou W, et al. Evaluation of rocking seismic isolation performance of railway tall piers with different energy dissipation devices. *Structures* 2023;56:104923.
- [21] Wei B, Tan H, Wan K, et al. Seismic performance of railway bridges with novel ductile piers under near-fault earthquakes. *Transp Geotech* 2024;46:101241.
- [22] Zhang C, Ali Amir. The advancement of seismic isolation and energy dissipation mechanisms based on friction. *Soil Dyn Earthq Eng* 2021;146:106746.
- [23] Sheikh Hediyyeh, Van Engelen Niel C, Ruparathna Rajeev. A review of base isolation systems with adaptive characteristics. *Structures* 2022;38:1542–55.
- [24] Qi Q, Shao C, Cui H, et al. Shaking table tests and numerical studies on the seismic behaviors of FPB in railway continuous beam bridges. *Eng Struct* 2023;290:116318.
- [25] Meng D, Hu S, Yang M, et al. Experimental evaluation of the seismic isolation effectiveness of friction pendulum bearings in bridges considering transverse pounding. *Soil Dyn Earthq Eng* 2023;170:107926.
- [26] Ghanbari B, Fathi M, Akhaviey AH. The effect of superstructure properties on the re-centering capability of friction pendulum (PS) isolator. *Structures* 2024;63:106508.
- [27] Jiang L, Yu K, Jiang L, et al. Effects of shear panel dampers on seismic response mitigation of high-speed railway simply supported bridge-track system under far-field and near-field ground motions. *Arch Civ Mech Eng* 2023;23:93.
- [28] Jiang L, Zhong B, Zhang Y, et al. A novel seismic-resistant design for track structures in the bridge-embankment transition zone of multi-span high-speed railways simply supported bridges. *Eng Struct* 2025;324.
- [29] Xiong L, Zhou W, Jiang L. Seismic risk transfer in multi-span simply supported beam bridges for high-speed railways. *Soil Dyn Earthq Eng* 2025;188:109057.
- [30] Zou S, Zhou Wen L. F. Shaking table test of a high-speed railway bridge with a new isolation system. *Eng Struct* 2019;196:109315.
- [31] Hu R, Hu S, Yang M, et al. Experimental study on the coordinated behavior of the Combined Viscous-Steel Damping System (CVSDS) for multi-level seismic mitigation. *Structures* 2023;57:105344.
- [32] Xu X, Chen X, Hu H, et al. Energy dissipation and seismic response reduction system for high-speed railway bridges based on multiple performance requirements. *Eng Struct* 2024;307:117919.
- [33] Zhuang P, Zhao W, Zhang G, et al. Shaking table tests on seismic behaviors of a single-layer spherical lattice shell with shape memory alloy-controlled friction pendulum bearings. *J Build Eng* 2023;82:108150.
- [34] Yu J, Jiang L, Zhou W, et al. Running test on high-speed railway track-simply supported girder bridge systems under seismic action. *Bull Earthq Eng* 2021;19(9):3779–802.
- [35] Yu J, Zhou W, Jiang L, et al. Design seismic track irregularity for high-speed railways. *Earthq Eng Struct Dyn* 2023;52(15):4865–83.
- [36] Tondini N, Stojadinovic B. Probabilistic seismic demand model for curved reinforced concrete bridges. *Bull Earthq Eng* 2012;10:1455–79.
- [37] Tran-Ngoc H, He Leqia, Reynders Edwin, et al. An efficient approach to model updating for a multispan railway bridge using orthogonal diagonalization combined with improved particle swarm optimization. *J Sound Vib* 2020;476:115315.
- [38] Kazemi F, Asgarkhani N, Jankowski R. Optimization-based stacked machine-learning method for seismic probability and risk assessment of reinforced concrete shear walls. *Expert Syst Appl* 2024;255:124897.
- [39] Li D, Ye Z, Lu P, et al. Reliability intelligence analysis of concrete arch bridge based on Kriging model and PSOSA hybrid algorithm. *Artif Intell Rev* 2023;56:2667–85.
- [40] Kazemi F, Asgarkhani N, Jankowski R. Machine learning-based seismic fragility and seismic vulnerability assessment of reinforced concrete structures. *Soil Dyn Earthq Eng* 2023;166:107761.
- [41] Kazemi F, Asgarkhani N, Jankowski R. Machine learning-based seismic response and performance assessment of reinforced concrete buildings. *Arch Civ Mech Eng* 2023;23(2).